

## Using DTSA-II to Simulate and Interpret Energy Dispersive Spectra from Particles

Nicholas W.M. Ritchie

*Surface and Microanalysis Science Division, Chemical Science and Technology Laboratory, National Institute of Standards and Technology, 100 Bureau Drive, MS: 8371, Gaithersburg, MD 20899-8371, USA*

**Abstract:** A high quality X-ray spectrum image of a 3.3  $\mu\text{m}$  diameter sphere of K411 glass resting on a copper substrate was collected at 25 keV. The same sample configuration was modeled using the NIST Monte Carlo simulation of electron and X-ray transport as is integrated into the quantitative X-ray microanalysis software package DTSA-II. The distribution of measured and simulated X-ray intensity compare favorably for all the major lines present in the spectra. The simulation is further examined to investigate the influence of angle-of-incidence, sample thickness, and sample diameter on the generated and measured X-ray intensity. The distribution of generated X-rays is seen to deviate significantly from a naive model which assumes that the distribution of generated X-rays is similar to bulk within the volume they share in common. It is demonstrated that the angle at which the electron beam strikes the sample has nonnegligible consequences. It is also demonstrated that within the volume that the bulk and particle share in common that electrons, which have exited and later reentered the particle volume, generate a significant fraction of the X-rays. Any general model of X-ray generation in particles must take into account the lateral spread of the scattered electron beam.

**Key words:** microanalysis, particle, Monte Carlo, simulation, spectrum imaging, X-ray

### INTRODUCTION

Quantitative X-ray microanalysis of particles is a challenge. Even for bulk samples, the weight fraction of an element is not simply proportional to the intensity of the emitted X-rays. Numerous schemes have been developed to compensate for differences in backscattered fraction, electron stopping power, X-ray absorption, and secondary fluorescence. These schemes make assumptions about the shape, homogeneity, and orientation of the sample. Unfortunately, these assumptions typically do not hold for microparticles.

Quantitative analysis of flat, polished bulk samples is tractable because the geometry is well defined. With the exception of backscattered electrons, the energetic electrons are fully contained within the volume of the sample. The absorption path length, the distance from the point of generation through the intervening sample to the detector, is easy to calculate. On the other hand, the geometry of particles is typically not fully known. It is usually possible to determine the projected area of the particle in the plane perpendicular to the electron beam. Determining the height profile and the thickness of the particle is less easy using an electron beam instrument.

If the shape of a particle is well known, it is presumably possible to build a model and estimate the necessary quantitative corrections. There are, however, few examples of microparticles for which the full shape and composition are fully characterized. National Institute of Standards and Technology (NIST) SRM-2066 represents one such example. SRM-2066 consists of an ensemble of roughly spherical particles of K411 glass. The composition of K411 (which is itself part of SRM-470) is established by the mass fraction of the constituent materials and by subsequent analysis. The composition of SRM-2066 is certified by NIST (see [https://www-s.nist.gov/srmors/view\\_detail.cfm?srm=2066](https://www-s.nist.gov/srmors/view_detail.cfm?srm=2066)), as summarized in Table 1. The density of bulk K411 and, presumably, the SRM-2066 spheres is 2.95 g/cm<sup>3</sup>. The microspheres are constructed by grinding bulk glass into shards and then melting the shards in a low velocity air stream in an oven at 1350°C. The spheres thus produced are observed to have generally spherical shape and smooth surface texture. The spheres range in diameter from approximately 1 to 50  $\mu\text{m}$ .

This article represents a detailed study of X-ray emission from a single microparticle. The study involves the measurement of a high quality X-ray spectrum image and a Monte Carlo simulation of the same. The goal of this study is to use a Monte Carlo simulation to investigate the various different phenomena that differentiate the distribution of X-ray generation in particles from in bulk. The first step is

**Table 1.** Composition of SRM-2066 K411 Microspheres and Bulk K411 Glass as Specified in the NIST SRM-2066 Certificate.\*

Element	SRM-2066 Value (weight fraction)	Bulk Glass Value (weight fraction)
Silicon	0.256 ± 0.017	0.2538 ± 0.0090
Calcium	0.112 ± 0.023	0.1106 ± 0.0014
Magnesium	0.092 ± 0.014	0.0885 ± 0.0012
Iron	0.112 ± 0.023	0.1121 ± 0.0016
Oxygen	0.429 ± 0.012	0.4239 ± 0.0024

\*The nominal density of K411 glass is 2.946 g/cm<sup>3</sup>.

to demonstrate that the Monte Carlo simulation can reproduce the gross features of spectra collected from a spherical particle by comparing a simulated and a measured X-ray spectrum image. The Monte Carlo will then be used to further investigate various phenomena that we suspect contribute to the differences between bulk and particle spectra. These differences include effects due to excitation volume, electron loss, absorption path, nonnormal incidence, backscatter from the substrate, and scatter from the particle. These effects are hard to investigate experimentally, but each must be understood to develop a sophisticated credible model for quantifying particle spectra.

## MATERIALS AND METHODS

The X-ray spectrum image was collected on JEOL JXA-8500F (JEOL Ltd., Tokyo, Japan), thermal field emission microprobe, using a Bruker 4040 (Bruker AXS Inc., Madison, WI, USA) silicon drift detector (SDD).<sup>a</sup> The JEOL JXA-8500F is a highly stable instrument. On ideal conductive samples, the JXA-8500F is capable of less than 100 nm drift per hour. The probe current drift over similar time periods is less than 0.1%. The thermal field-emission gun is capable of high brightness. The diameter of the probe is estimated to be on the order of or smaller than the pixel dimensions (~30 nm<sup>2</sup>) at 5 nA probe current. The stability and brightness make the system ideal for collecting high count, high-resolution X-ray maps of microparticles.

The SDD is mounted at an azimuthal angle of 150° with respect to the stage axes. To facilitate interpretation and to minimize the effect of spatial drift, the raster was rotated to align the scan rows parallel to the detector azimuth. A rectangular map shape of pixel dimensions 160 H × 120 V was selected to cover the area of the particle plus

<sup>a</sup>Certain products, both public domain and commercial, are identified in this article. Identification of such products does not imply recommendation or endorsement by NIST, nor does it imply that the identified product is the best available.

**Table 2.** Ionization Ranges with  $E_0 = 25$  keV in K411 and Bulk Copper for the Various Shells Contributing to X-Rays (Kanaya & Okayama, 1972).

Atomic Shell	Range ( $\mu\text{m}$ )	Atomic Shell	Range ( $\mu\text{m}$ )
O K	5.36	Fe K	4.71
Mg K	5.33	Fe L <sub>3</sub>	5.36
Si K	5.3	Cu K	1.73
Ca K	5.12	Cu L <sub>3</sub>	2.1

some of the shadow. Each scan of a row took approximately 30 s during which time beam drift was found to be negligible. This was verified by observing the registration of the edges of the particle on adjacent scan rows.

The map was collected at 25 keV and 5.0 nA. The raster was configured for 0.2 s per pixel and an output count rate of approximately 60 kcps. The SDD is a four-element detector so each detector had an output count rate of approximately 15 kcps. The detectors were configured for the optimal resolution of about 125 eV at Mn K $\alpha$ .<sup>b</sup> 15 kcps, a modest count rate for this detector, was selected to minimize coincidence events and thus to enhance the quantitative nature of the map. Higher probe currents were also observed to increase charging leading to beam drift and occasionally to cause electrostatic particle loss (“pinging”).

A 3.3  $\mu\text{m}$  particle was selected based on roundness, homogeneity, and diameter similar but smaller than the ionization range for the constituent elements at 25 keV incident beam energy (see Table 2). The size selection and beam energy are understood to be suboptimal for quantitative analysis but were selected because they show a richness of phenomena that ultimately influence the quantitative analysis of particles.

The particle was homogeneous to the limits of our ability to observe. We made earlier measurements with particles from a different batch of K411 microspheres in which inhomogeneity was clearly evident in the iron and calcium signals on the 50–100 nm spatial scale as evident in Figure 1.

The particle was mounted on a crossbar of a Cu transmission electron microscope grid. While this substrate is suboptimal for quantification due to the mismatch between mean atomic numbers, the substrate provides two interesting line families for study—the high energy Cu K family between 8 and 9 keV and the low energy Cu L family at about 1 keV. See Table 3 for a summary of the mass absorption coefficients for Cu lines by K411. Furthermore, bulk copper will produce an X-ray signal that is easy to

<sup>b</sup>Siegbahn notation is used to identify groups of transitions and IUPAC notation to identify specific transitions (IUPAC K-L3 is equivalent to Siegbahn K $\alpha$ 1).

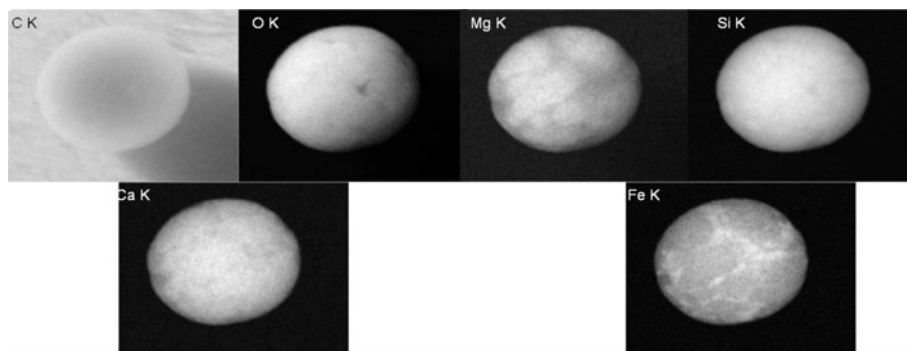


**Figure 1.** X-ray maps from a  $3\ \mu\text{m}$  sphere of inhomogeneous K411 glass on a carbon substrate. This sphere was from a different batch than that in Figure 2. These maps demonstrate that inhomogeneity of the scale of tens to hundreds of nanometers can be resolved using a bright 25 keV probe.

**Table 3.** Mass Absorption Coefficients for the Major X-Ray Lines Represented in K411 Glass and the Copper Substrate (Chantler et al., 2005).\*

Line IUPAC	Siegbahn	Material	Coefficient ( $\text{cm}^2/\text{g}$ )	$1/e$ Range ( $\mu\text{m}$ )
Cu K-L3	Cu $K\alpha 1$	K411	76	44.6
Cu L3-M5	Cu $L\alpha 1$	K411	4,651	0.73
O K-L3	O $K\alpha 1$	K411	5,666	0.6
Mg K-L3	Mg $K\alpha 1$	K411	2,132	1.59
Si K-L3	Si $K\alpha 1$	K411	1,113	3.05
Ca K-L3	Ca $K\alpha 1$	K411	271	12.5
Fe K-L3	Fe $K\alpha 1$	K411	87.6	38.7
Fe L3-M5	Fe $L\alpha 1$	K411	7,175	0.47
Cu K-L3	Cu $K\alpha 1$	Cu	48	23
Cu L3-M5	Cu $L\alpha 1$	Cu	1,515	0.74

\*The  $1/e$  lengths assume a density of  $2.946\ \text{g}/\text{cm}^3$  for K411 and  $8.96\ \text{g}/\text{cm}^3$  for pure copper.

model and can produce informative structure in the X-ray spectrum image.

The resulting X-ray spectrum image was processed using LISPIX (available from <http://www.nist.gov/lispix/>) to produce the X-ray intensity maps shown in Figure 2a. The maps are not background corrected.

## RESULTS

### Measured Spectrum Image

There are many interesting phenomena evident in these maps. The O K map clearly shows the effects of X-ray absorption. The generation of X-rays is radially symmetric about the center of the particle. The detected emission is not. The right side of the particle is less bright than the left

side—the left side being closest to the detector. This suggests that for O K absorption is a significant influence. The fact that the particle is not completely dark on the Cu L image shows that electrons which initially impact the sphere often eventually strike Cu. The fact that the right side of the particle is not dark suggests that some of the electrons that strike the backside of the particle scatter out of the shadow. The darkest point on the particle is the top—the point at which electrons are least likely to side scatter and must travel through the most material to interact with the substrate. Behind the particle, however, is dominated by a Cu L shadow. Cu L X-rays produced here are absorbed by the particle before they can reach the detector. It is possible to use the shape of the shadow to estimate the shape of the particle as seen from the perspective of the detector. The Mg K and Si K maps are similar to the O K although the absorption is less strong and less evident except at the farthest points from the detector. Si K and Ca K are probably the best images to observe the effect of sample thickness. The Si K and Ca K maps are brightest at the center of the particle and diminish as the beam traverses to the edges. The absorption path length for Ca K exceeds the diameter of the particle. The emission images are basically radially symmetric about the center of the particle. The count statistics on the Fe K are poor, and this image looks particularly speckled. However, even at the very edges of the particle there is still a fairly substantial Fe K X-ray intensity. This suggests that many of the electrons that strike the particle even at a glancing angle will scatter into the particle and generate X-rays. The Cu K image is strikingly different from the Cu L. The center of the particle is dark, and the edges show some Cu K intensity. The darkness at the center suggests that electrons rarely make their way through the particle with sufficient energy to ionize the Cu K shell at 8.98 keV. The Cu K intensity around the edges could be attributed either to side scatter or to electrons traversing the diminished thickness. These two causes are really just two different extremes of the same phenomena—electrons scat-

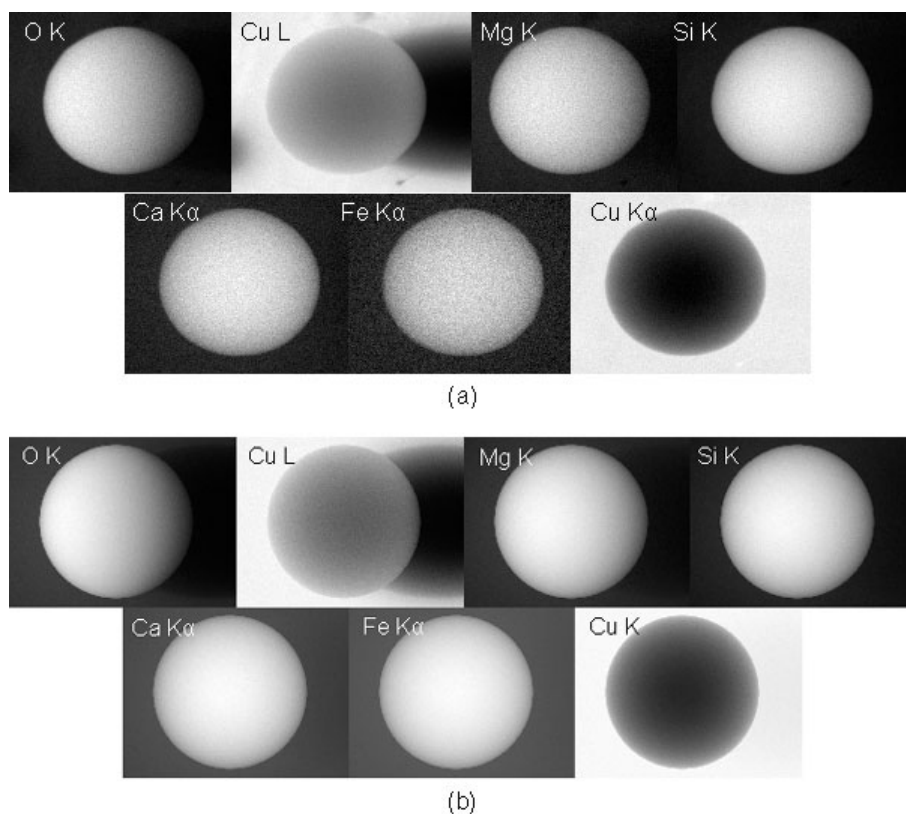


**Figure 2.** X-ray maps collected from a single K411 microsphere of  $3.3\ \mu\text{m}$  diameter mounted on a copper grid using an electron probe energy of 25 keV. The detector is to the left at a  $35^\circ$  elevation. **a:** X-ray maps derived from the measured spectrum image. **b:** The equivalent X-ray maps derived from the Monte Carlo simulated spectrum image.

tering out of the particle. The distinction is simply the number of scattering events before the particle escapes, and in reality electrons are rarely backscattered with a single elastic collision.

### Monte Carlo Simulations

The second part of this article applies the NISTMonte Monte Carlo simulator of electron and X-ray transport as integrated into DTSA-II (available from <http://www.cstl.nist.gov/div837/837.02/epq/dtsa2/index.html>) to investigate and interpret these various observations. The implementation of the NISTMonte Monte Carlo simulator is documented elsewhere (Ritchie, 2005, 2009). In overview, NISTMonte computes the trajectories of electrons in complex three-dimensional shapes of arbitrary materials using a Mott elastic scattering model and energy loss modeled using the continuous slowing down approximation. At each elastic scattering point, the probability is calculated that an ionization occurred in the segment between this scattering point and the previous one. The probability of ionization combined with X-ray emission relaxation rates is used to compute the intensity of X-rays emitted over the trajectory segment. This intensity is attributed to one point selected at

random along the length of the segment and the X-ray intensities tracked back to the detector through all intervening material. The detector model records the unabsorbed fraction. The detector model is designed to realistically simulate laboratory detectors including geometry, materials, windows, and response. The detector model used in this study was configured to emulate the Bruker 4040 and, as Figure 3 demonstrates via comparison between a measured bulk K411 and a simulated K411 spectra, produces credible simulated spectra from first principles. The poorest agreement is at the lowest energies where absorption plays the strongest role. The intensity was refined slightly by adjusting the simulated distance from sample to detector. This quantity is poorly known, and the value used (72 mm) is within 10% of our best estimate from instrument and detector vendor drawings.

The Monte Carlo was configured with a model of the sample, electron probe, and detector that closely matched the configuration used to collect the X-ray spectrum images in Figure 2a. Listing 1 shows the DTSA-II Python script. The script iterates through each pixel in the  $160 \times 120$  spectrum image and follows the trajectory of 1,000 electrons. Like the experiment we model, it is the position of the electron beam that defines the pixel, not necessarily the

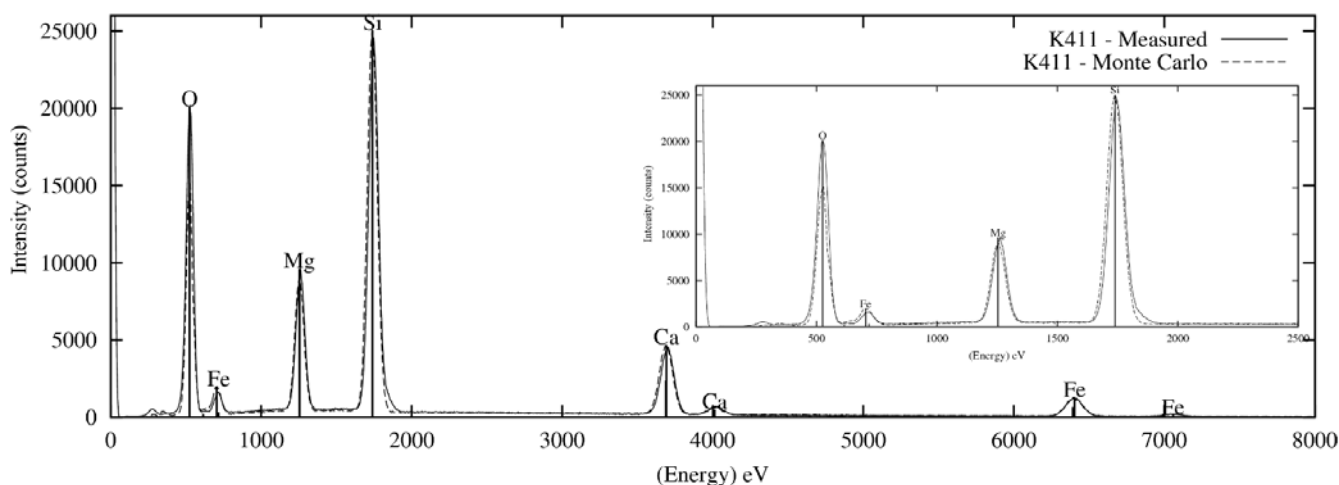


**Figure 3.** Comparing measured and Monte Carlo simulated spectra from bulk K411 glass. The Monte Carlo gets the absolute intensity scale approximately correct, but the sample-detector distance for the simulation has been adjusted by <10% for the optimal agreement.

source of the X-rays. Since each electron scatters hundreds of times, this number of electrons proves sufficient to produce precise, reproducible spectra. In addition to saving the spectra in individual MSA standard spectrum files, the spectra are also recorded in LISPIX ripple/raw files—the same format as the measured spectrum image. The simulated spectra were processed in the same manner as the measured spectra to produce the intensity maps shown in Figure 2b. The most immediate difference observed between Figures 2a and 2b is the level of noise between adjacent pixels. The spectra in Figure 2a are limited by a 0.2 s acquisition at 5 nA producing a 60,000 cps output count rate and approximately 12,000 counts per pixel. The spectra in Figure 2b are limited in precision by the fact we only followed 1,000 electron trajectories. Clearly, the simulation produces smoother images. We can readily account for the difference in dose by rescaling the simulated spectra and simulating Poisson noise as appropriate for the experimental dose (1 nA · s).

## DISCUSSION

When we look closer we see that the simulations reproduce all the gross phenomena discussed for the measured spectra. Figure 4 makes this observation more quantitative. LISPIX provides many tools for interrogating the spectrum image. One tool allows us to plot the integrated intensities along the axis of a chord through the image. If we take a chord horizontally through the center of the particle as shown in the lower left corner of Figure 4 and plot the intensities, we get the traces in Figure 4. Most of the interesting behavior occurs parallel to the detector axis. The intensity of the simulated

spectra has been rescaled individually such that the average measured and simulated intensities are equal in the integrated strip. These plots demonstrate that the simulation is capable of quantitatively reproducing all the phenomena discussed earlier. The agreement among the elements present in the particle is particularly good while there are some differences between the copper traces.

The O K trace is dominated by absorption, and the simulation gets the shape of this correct, suggesting that the distribution of positions of emission and the absorption are modeled roughly correctly. The leading edge of the O trace is nonzero because of electrons that backscatter from the copper and strike the particle and because of the bremsstrahlung background. On the trailing edge, the trace is lower than the leading edge because of absorption by the intervening particle.

Each of the Mg K, Si K, Ca K-L<sub>3</sub>, and Fe K-L<sub>3</sub> traces become increasingly symmetric, which is characteristic of a decreasing influence of absorption effects.

The Cu lines are more difficult to model particularly within the particle volume because they depend so critically on so many different parameters and result from later events in the trajectory of the electron. The Cu radiation in the particle region results from electrons that have bounced around the K411 particle exited and struck the copper. The scattered electrons strike the copper at nonnormal incidence, and thus the emission distribution will be shallower than that due to an electron with the same energy incident normal to the surface. The distribution of incident electron energies will depend on the position of the beam on the sample.

We can also compute the  $\varphi(\rho z)$  curve for each pixel in the map. The  $\varphi(\rho z)$  curve represents the ionizations within a specific shell as a function of depth relative to the ioniza-

```

# K411 sphere on Cu.py - DTSA-II Python script
# A script for computing an x-ray spectrum image of a K411 glass
# sphere on a copper substrate.
# Author:          Nicholas W. M. Ritchie
# Last modified:   9-Feb-2009

# Define the materials
k411 = epq.Material(epq.Composition([epq.Element.Ca, epq.Element.Fe, epq.Element.O,
                                   epq.Element.Mg, epq.Element.Si],
                                   [0.112, 0.112, 0.429, 0.092, 0.256] ),
                  epq.ToSI.gPerCC(2.946))

k411.setName("SRM-2066")
c = epq.MaterialFactory.createPureElement(epq.Element.Cu)

# Place the sample at the optimal location for the detector
det = findDetector("Bruker 10")
origin = epu.Math2.multiply(1.0e-3, epq.SpectrumUtils.getSamplePosition(det.getProperties()))

e0=25.0          # beam energy (keV)
partDiameter = 3.3e-6 # particle size (meters)
size = [ 160, 120 ] # map dimensions
center = [ 76, 59 ] # particle center (pixels)
stride = [ 4, 2 ] # split the task up to run on multiple CPUs

# Bookkeeping
r = 0.5*partDiameter # particle radius
pixSize = (2*r)/108.3 # edge length of a single pixel (meters)
dose = 150.0e-9 # A*sec
nTraj = 1000 # electrons
# Output files
path="%s/%s_[%d,%d].%s" % ( DefaultOutput,k411,offset % stride[0], offset / stride[0],"%s")
res = ept.RippleFile(size[0],size[1],depth,ept.RippleFile.SIGNED,4,ept.RippleFile.DONT_CARE_ENDIAN,
                    path % "rpl", path % "raw")
# Iterate over each pixel in the spectrum image
for x in range(offset % stride[0], size[0], stride[0]):
    if terminated:
        break
    for y in range(offset / stride[0], size[1], stride[1]):
        if terminated:
            break
        det.reset() # clear the detector accumulator
        monte = nm.MonteCarloSS()
        gun=nm.GaussianBeam(1.0e-9)
        gun.setCenter([(x-center[0])*pixSize, (center[1]-y)*pixSize,-0.01])
        monte.setElectronGun(gun)
        monte.setBeamEnergy(epq.ToSI.keV(e0))
        # Create a sphere of k411
        center = epu.Math2.plus(origin, [0.0,0.0,r])
        monte.addSubRegion(monte.getChamber(), k411, nm.Sphere(center,r))
        # Place it on a carbon substrate
        monte.addSubRegion(monte.getChamber(), c, nm.MultiPlaneShape.createSubstrate([0.0,0.0,-1.0],
            epu.Math2.plus(origin, [0.0,0.0,2*r])) )
        # Add event listeners to model characteristic and Bremsstrahlung radiation
        xrel=nm.XRayEventListener2(monte,det)
        monte.addActionListener(xrel)
        brem=nm.BremsstrahlungEventListener(monte,det)
        monte.addActionListener(brem)
        # Run the MC
        monte.runMultipleTrajectories(nTraj)
        # Get the spectrum and assign properties
        spec=det.getSpectrum(dose / (nTraj * epq.PhysicalConstants.ElectronCharge))
        res.seek(y, x)
        res.write(epq.SpectrumUtils.toIntArray(spec)[0:2048])
        # Write the spectrum to disk and display
        fos = jio.FileOutputStream("%s/%s[%d,%d].msa" % (DefaultOutput, k411, x, y))
        ept.WriteSpectrumAsEMSA1_0.write(spec, fos, 0)
        fos.close()
res.close() # close the ripple file

```

**Listing 1.** A script for generating an X-ray spectrum image for the 3.3  $\mu\text{m}$  sphere of K411 on a Cu substrate. The scripts used to generate the results presented here are available from [http://dtsa2.svnrepository.com/DTSA2\\_Scripts/trac.cgi/browser/NWMR%20EMSA-2009](http://dtsa2.svnrepository.com/DTSA2_Scripts/trac.cgi/browser/NWMR%20EMSA-2009).

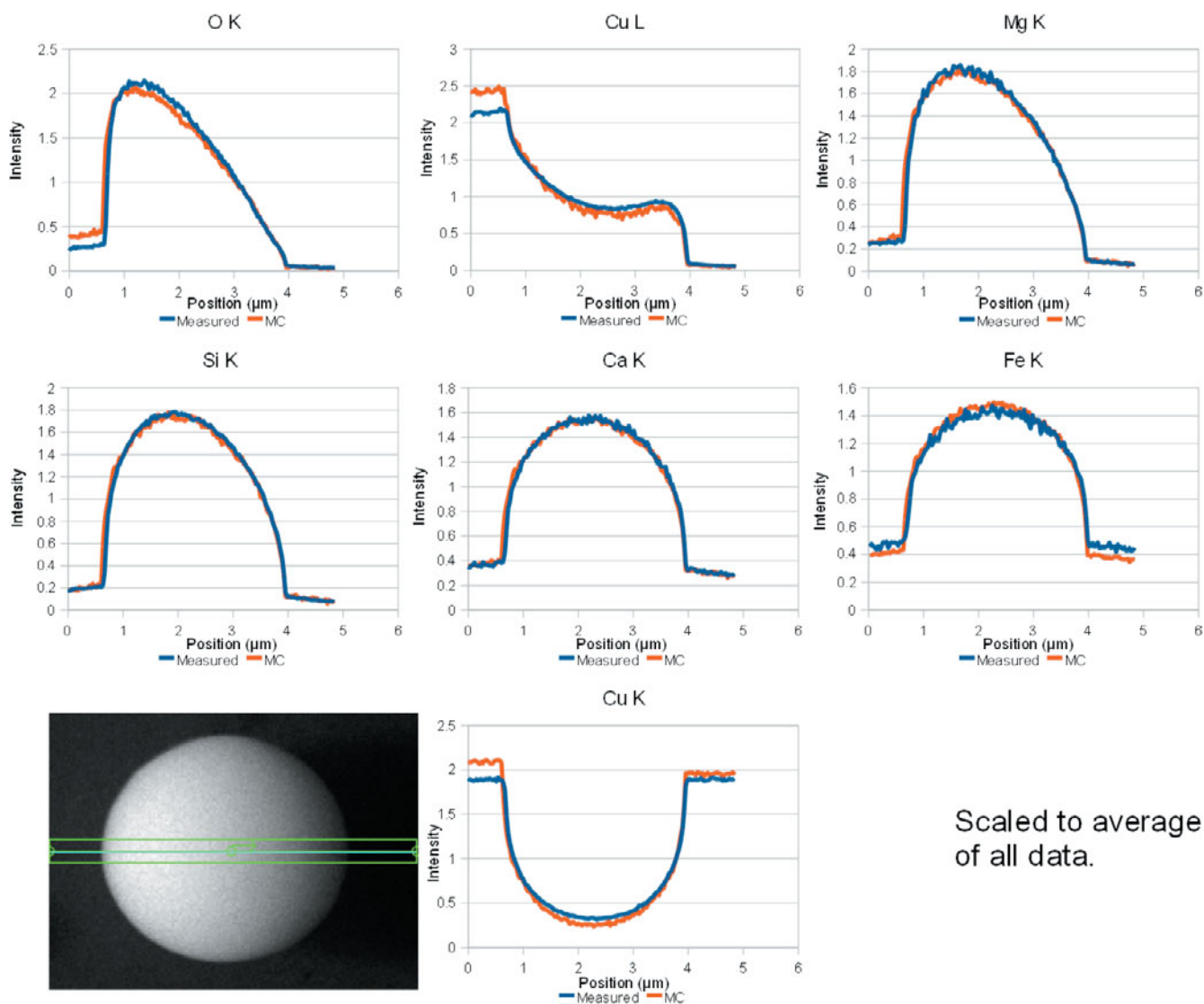


**Figure 4.** Plots of the intensities of various different X-ray lines as a function of horizontal position. The particle image at the bottom shows the position and width of the region integrated to produce the plots. The intensity of the simulated spectra was scaled to produce the same average value as the measured spectra.

tions in the same shell in an infinitesimally thin film at the surface. While conventional, the  $\varphi(\rho z)$  curve is not the most useful way to present this information for our purposes. A better way is to plot either the generated X-ray intensity or emitted X-ray intensity as a function of depth. These plots show the absolute magnitude of X-rays generated/emitted rather than just the relative magnitude. Figure 5a shows the generated X-ray intensity in the O K-L<sub>3</sub> line as a function of depth for 12 different points along a radial from the center of the particle. The points are chosen in a linear progression where 0% represents the center of the particle and 100% represents the full radius of the particle. Some of the electrons at the 100% point strike the particle because the incident beam is modeled with a 1 nm Gaussian width. The 110% point fully misses the particle

but some of the electrons backscatter from the substrate to the particle to generate X-rays. The generation curves are symmetric with respect to rotation about the center of the radially symmetric particle. The detected X-ray emission, however, is a function of the azimuthal angle due to differences in absorption path length. The absorption path length can be calculated analytically for each azimuthal point and applied to the generated intensities. The symmetry for spheres and other radially symmetric particle shapes can be used to optimize the calculation of the full X-ray map.

Factoring the problem into generation and absorption allows us to consider generation and the factors that influence generation independent of absorption. The generation of X-rays in a spherical particle is different from generation

Scaled to average of all data.

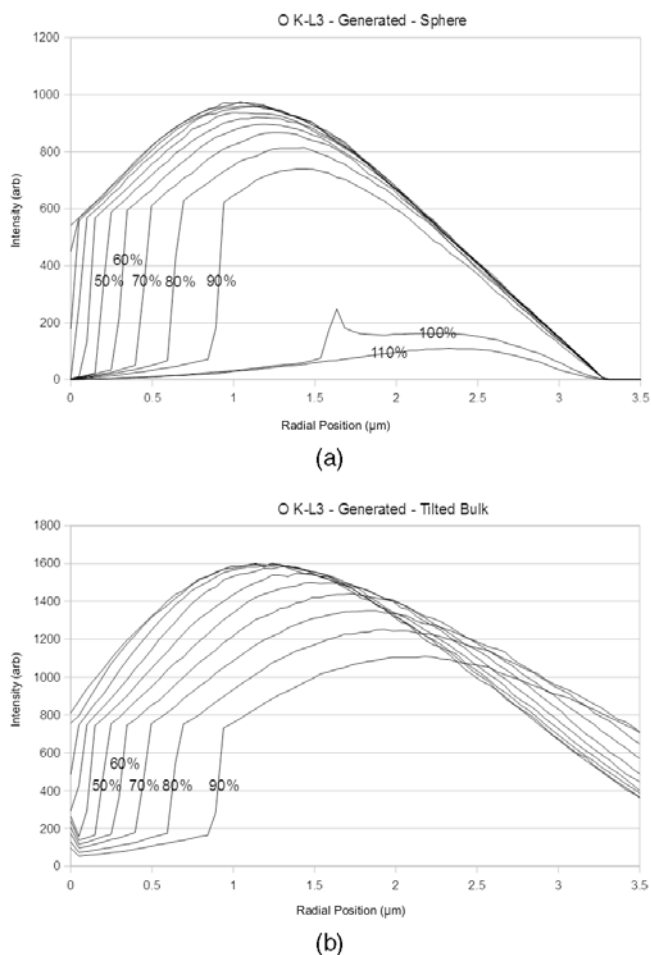
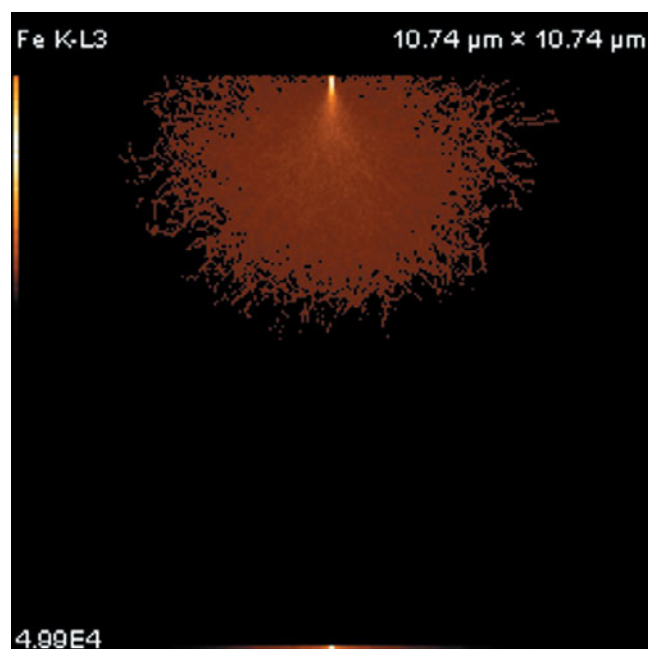


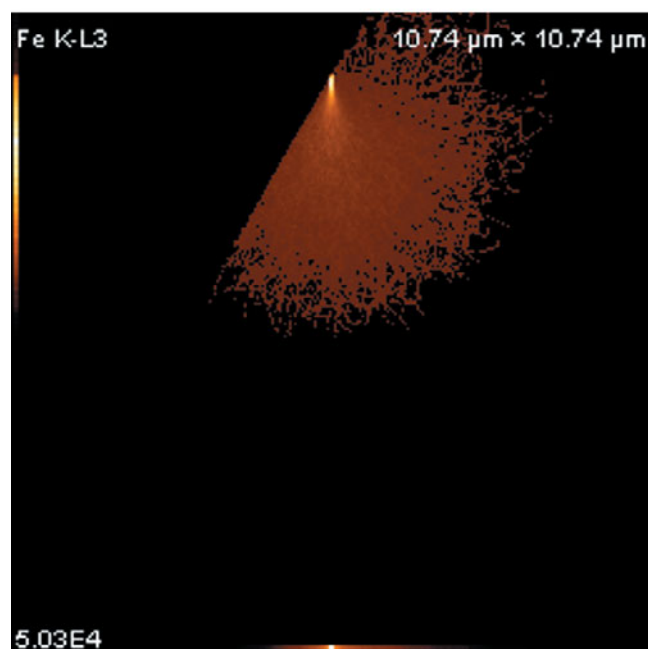
**Figure 5.** Comparing the generated O K-L<sub>3</sub> (a) X-rays generated from various positions on the radius of the sphere with (b) X-rays generated on a bulk sample tilted to a comparable angle. The curves are labeled according to the corresponding distance from the center of the sphere to the radius. Curves below 50% are not labeled but can be readily deduced from the sequence. The point of incidence for the sphere drops as a consequence of the curvature of the sphere. The point of incidence on the tilted sample is offset to mimic the sphere. Both show two distinct regimes—above and below the point of incidence. Above the point of incidence, X-rays are generated by electrons that have scattered back above the point of incidence. These electrons would be backscattered in a bulk sample oriented normal to the electron beam.

in bulk primarily due to differences in angle-of-incidence, mass depth, volume, and backscatter.

As the beam moves away from the center of the particle, the angle at which the beam strikes the sample varies from normal to glancing as  $\theta(R) = \arcsin(R/r)$  for  $0 \leq R < r$ . Figures 5 and 6 show the effect of angle on X-ray generation. Figure 6a shows the electron beam striking the sample normal to the surface. The electron beam enters the sample at the central bright point and scatters into a bulb shaped volume before losing sufficient energy to no longer



(a)



(b)

**Figure 6.** Comparing the electron beam striking the sample (a) at normal incidence with the beam striking (b) at an angle of 60°. At 60°, the beam penetrates as deep as normal incidence. However, electrons above and to the right of the point of incidence do not backscatter out of the sample. Electrons to the left of the point of incidence side scatter. Finally, the absorption path length is on average smaller because the X-rays are generated close to the surface by a factor of approximately  $\cos(\theta)$ , where  $\theta = 0$  is normal incidence.

excite X-rays. What Figure 6a omits showing are the electrons that backscatter out of the sample. These electrons undergo an approximately  $180^\circ$  change in direction and exit through the top face of the material. Typically approximately 5 to 50% of the incident electrons (dependent on mean  $Z$ ) eventually backscatter. Figure 6b shows an electron beam with the same properties striking the sample at an angle of  $60^\circ$ . The volume into which the electrons scatter is similar to normal incidence. However, electrons that scatter out of the sample on the upper left edge are lost. Electrons that would have backscattered to the right of the entry point are retained in the material, and some X-rays are actually generated above the point at which the electron beam enters the sample.

Figure 5 demonstrates this in more detail. Figure 5a shows the distribution of generated O K-L<sub>3</sub> X-rays as a function of the radial position on the spherical particle. At 0%, the center of the particle, X-rays are generated all the way from the top of the particle to the bottom in a smooth distribution. As the beam steps out toward the edge, the point of incidence drops due to the curvature of the top surface of the particle. Below the point of incidence, the generation smoothly reaches a peak and then decreases to zero at the bottom of the particle. Above the point of incidence, X-rays are generated. These are due to the electrons that would have backscattered on a flat sample. Even at 110% of the particle radius, there is O K-L<sub>3</sub> signal due to electrons backscattering from the substrate even though the beam only strikes the substrate and the substrate contains no oxygen.

For comparison, Figure 5b shows the generation of X-rays as a function of depth for tilted bulk samples. The tilts are chosen to match the angle of the surface on the sphere at the various different distances from center and are labeled according to the correspondence. The vertical point of at which the beam strikes the sample is held constant to better match the sphere. These plots show the same behavior above and below the point of incidence as in Figure 5a. Above and below the point of incidence, the generation continues further than the spherical case. As reported in Table 2, the ionization range for the O K shell is  $5.36 \mu\text{m}$  for K411 at  $E_0 = 25 \text{ keV}$ .

To further interpret the differences between Figures 6a and 6b, it helps to divide the sphere into slices of equal thickness in the vertical dimension. If the sphere is of radius  $R$  and centered at the origin, then the volume of these slices is approximately the thickness of the slice,  $\Delta z$ , times the area, or  $V(z) = \pi(R^2 - z^2) \cdot \Delta z$ . The slices describe the volume from which particle X-rays can be emitted. If we consider any one of these slices, it helps intuition to consider that the generation of X-rays within the slice is made up from two different contributions. The first contribution is made by those electrons with generally the same trajectory as the incident electrons. These electrons have not undergone many scattering events. This contribution diverges as it progresses through the particle. The second

contribution is from those electrons that have undergone significant scattering events. In the slices near the incident point, the generation of X-rays is dominated by those electrons that have undergone few scattering events. This is demonstrated for the O K-L<sub>3</sub> X-ray in bulk K411 in Figure 7. The slices nearest the surface are dominated by the central lobe from the localized incident beam. Multiply scattered electrons dominate slices deep into the material. It is worth noting that in the case considered here the width of the volume from which X-rays are generated is larger than the radius of the particle. This implies that electrons will escape out the sides of the particle as well as the bottom. Any model that ignores the lateral extent of the generation of X-rays will overestimate the X-ray generation for two reasons. First, the generated intensity drops to zero outside the particle, and second, randomized electrons that exit the particle volume are substantially less likely to scatter back into the particle. This suggests that the bulk radial distribution will overestimate the equivalent particle distribution even inside the particle.

Figure 8 looks more closely at the radial distribution of generated X-ray intensity. Figure 8a looks at the generated intensity distribution as a function of outer radius of the annulus integrated over the full depth ( $z$ ) dimension. The emission from the sphere is strictly less than the emission from the bulk at all radii, but least so in the central cylinder. Figure 8b looks at the relative difference in generated intensity between the bulk and the sphere for various planes perpendicular to the incident beam axis. Zero percent represents equal intensity in sphere, and bulk 100% represents no intensity from the sphere. Close to the axis the generated intensity is similar. Closer to the edges of the sphere the difference increases and drops precipitously to 100% at the edge. The difference can be attributed to electrons that are lost out of the sphere, which in the bulk would have scattered back into the material. It is worth remembering that after a handful of scattering events, the direction of the incident electrons to a large extent has been randomized. Like the classic problem of the staggering drunk, each additional stagger (scatter) is on average likely to take the drunk (electron) further from the flagpole (beam axis) even if the staggers (scatters) are distributed isotropically. Occasionally, it is even possible for the drunk (electron) to return to the flagpole (beam axis) after the initial staggers (scatters) have taken it far from the flagpole (beam axis.)

Finally, it is worth noting that the slight negative result for [3.0, 3.6] for  $r < 0.25$  may be due to increased backscatter from the Cu substrate and/or random fluctuations characteristic of Monte Carlo simulations.

## CONCLUSIONS

---

This study serves to demonstrate many of the reasons why developing a  $\varphi(\rho z)$ -type algorithm for quantifying

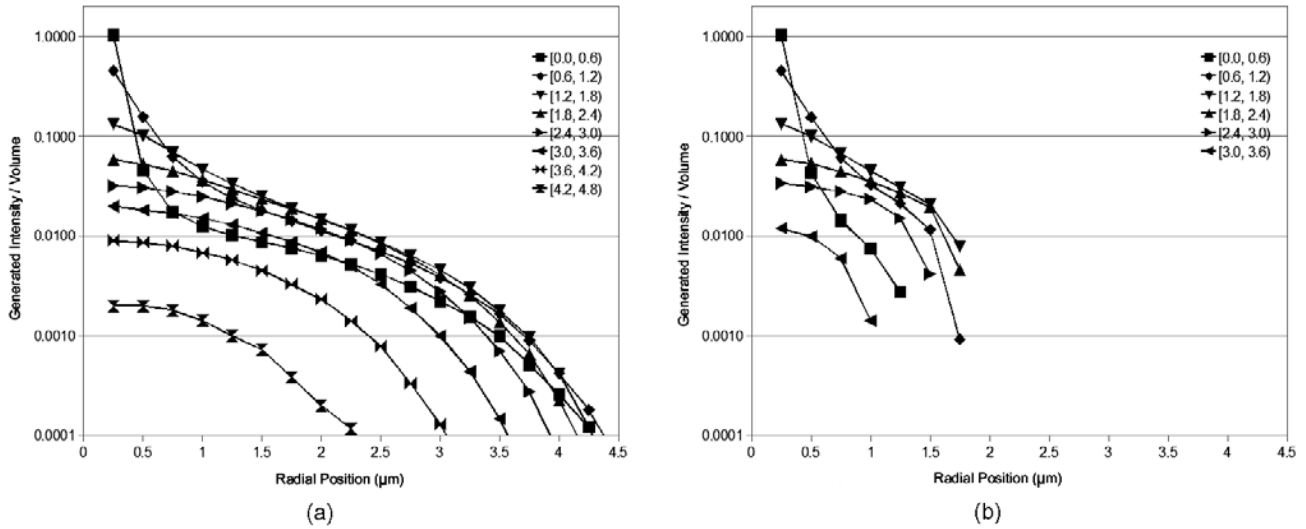


**Figure 7.** The radial distribution of O K-L<sub>3</sub> X-ray generation for various depths within (a) a bulk sample of K411 and (b) a 3.3 μm sphere of K411 for a probe incident on the symmetric axis of the particle. The horizontal axis represents the radial distance from the center of the particle in microns. The vertical axis represents the intensity per unit area on a logarithmic scale. The traces represent various different depth layers as identified by upper and lower boundaries in microns. The slice nearest the surface [0.0 μm, 0.6 μm] is peaked near the point of entry of the electron beam with a broad shoulder from backscattered electrons. As we go deeper into the sample, the peak due to the incident beam dissipates and the shoulder due to multiply scattered electrons begins to dominate. This behavior is seen in both the bulk and sphere case. In the bulk case, however, X-rays are generated from as far from the beam axis as 4 μm. In the sphere case, the X-rays are strictly limited to occur within the 1.65 μm radial extent of the particle.

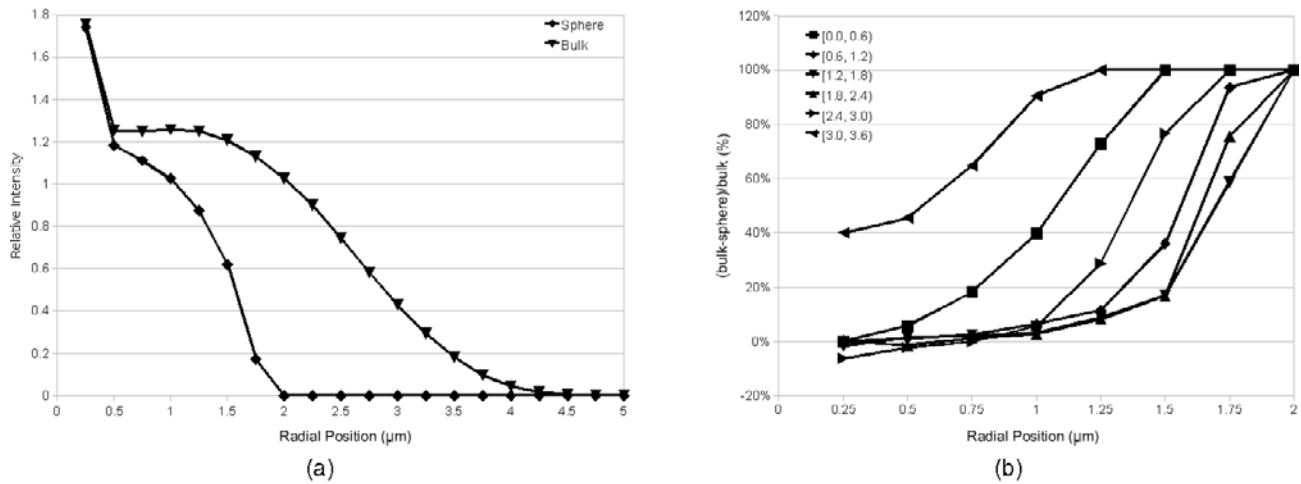


**Figure 8.** Comparing the distribution of O K-L<sub>3</sub> X-rays generated per unit area in cylindrical shells over a range of radii by a probe incident at the central symmetric axis. The abscissa represents outer diameter of the cylinder. The cylinder's inner diameter is the value of the next smaller abscissa (0 for the first point). **a:** Shows the intensity integrated over the entire vertical extent of the electron interaction. The total generated intensity at each distance from the beam axis is less in the sphere than in the bulk due to electron loss. **b:** Provides additional insight by subdividing the generated intensity into slices 0.6 μm thick by depth and by plotting the ratio of the difference between the intensity generated in bulk and the sphere by the intensity in the bulk. A value of 100% represents no emission in the sphere, and a value of 0% represents equal emission in the bulk and sphere. Some values drop below 0% because of the inherent variability in Monte Carlo simulations. Nearest the axis the difference between sphere and bulk is negligible except in the deepest slice ([3.0, 3.6]) only part of which falls within the sphere. As we get closer to the edge of the sphere, the difference increases as electrons scatter out of the sphere. If the electron trajectory ever takes the electron outside of the sphere, then it is essentially lost and is unlikely to generate further X-rays. The fraction of electrons that exits the equivalent volume in the bulk material and returns to produce X-rays is very small for interior shells.

particles is difficult. Armstrong has implemented a particle correction algorithm (Armstrong, 1991), which has proven quite successful. This algorithm uses a bulk  $\varphi(\rho z)$  that ignores the effect of incidence angle and does not account for the radial distribution of X-ray generation. Armstrong integrates the bulk  $\varphi(\rho z)$  curve over the volume of the particle with a simple factor to account for electrons exiting the side of the particle. Further study will be necessary to understand why this model is successful despite some of its less physical assumptions.

Monte Carlo simulation is probably our most powerful tool for understanding the complex phenomena that influence particle and other samples with complex geometries (Ro et al., 2003). As computers get faster and Monte Carlos more refined, it may turn out that using a Monte Carlo to correct particle spectra may be our most accurate method. Regardless, accurate  $\varphi(\rho z)$ -style algorithms will likely to continue to have a place for large ( $\sim 10,000$  particle) datasets collected using computer automated image/X-ray analysis and for providing the first estimate to seed the much less computationally efficient Monte Carlo algorithms.

## REFERENCES

---

- ARMSTRONG, J.T. (1991). Quantitative elemental analysis of individual microparticles with electron beam instruments. In *Electron Probe Quantification*, Heinrich, K.J.F. & Newbury, D.E. (Eds.), pp. 261–315. New York: Plenum Press.
- CHANTLER, C.T., OLSEN, K., DRAGOSET, R.A., CHANG, J., KISHORE, A.R., KOTOCHIGOVA, S.A. & ZUCKER, D.S. (2005). X-ray form factor, attenuation and scattering tables (version 2.1). Available at <http://physics.nist.gov/ffast> (March 29, 2010). Gaithersburg, MD: National Institute of Standards and Technology. Originally published as CHANTLER, C.T. (1995). *J Phys Chem Ref Data* **29**(4), 597–1048; and CHANTLER, C.T. (1995). *J Phys Chem Ref Data* **24**, 71–643.
- KANAYA, K. & OKAYAMA, S. (1972). Penetration and energy-loss theory of electrons in solid targets. *J Phys D* **5**, 43–58.
- RITCHIE, N.W.M. (2005). A new Monte Carlo application for complex sample geometries. *Surf Interface Anal* **37**, 1006–1011.
- RITCHIE, N.W.M. (2009). Spectrum simulation in DTSA-II. *Microsc Microanal* **15**, 454–468.
- RO, C.-U., OSÁN, J., SZALÓKI, I., DE HOOG, J., WOROBIEC, A. & VAN GRIEKEN, R. (2003). An expert system for chemical speciation of individual particles using low-Z particle electron probe X-ray microanalysis data. *Anal Chem* **75**, 851–859.